MDPI

Article

Deformation and Stress of Rock Masses Surrounding a Tunnel Shaft Considering Seepage and Hard Brittleness Damage

Zhenping Zhao [1], Jianxun Chen [2,*], Tengfei Fang [2], Weiwei Liu [2], Yanbin Luo [2], Chuanwu Wang [2], Jialiang Dong [1], Jian Li [1], Heqi Wang [1,2] and Dengxia Huang [1]

[1] CCCC Central South Engineering Bureau Co., Ltd., Changsha 410000, China
[2] School of Highways, Chang'an University, Xi'an 710064, China; 2022021048@chd.edu.cn (T.F.)
* Correspondence: chenjx1969@chd.edu.cn

Abstract: The mechanical and deformation behaviors of the surrounding rock play a crucial role in the structural safety and stability of tunnel shafts. During drilling and blasting construction, seepage failure and hard brittleness damage of the surrounding rock occur frequently. However, previous discussions on stress deformation in the surrounding rock did not consider these two factors. This paper adopts the theory of elastoplastic to analyze the effects of seepage and hard brittleness damage on the stress and deformation of the surrounding rock of a tunnel shaft. The seepage effect is equivalent to the volumetric force, and a mechanical model of the surrounding rock considering seepage and hard brittleness damage was established. An elastoplastic analytical formula for surrounding rock was derived, and its rationality was verified through numerical examples. Based on these findings, this study revealed the plastic zone as well as stress and deformation laws governing the behavior of surrounding rock. The results showed that the radius of a plastic zone had a significant increase under high geostress conditions, considering the hard brittleness damage characteristics of the surrounding rock. The radius of the plastic zone increased with an increase in the initial water pressure and pore pressure coefficient, and the radius of the plastic zone increased by 5.5% and 3.8% for each 0.2 MPa increase in initial water pressure and 0.2 increase in pore pressure coefficient, respectively. Comparing the significant effects of various factors on the radius of the plastic zone, the effect of support resistance inhibition was the most significant, the effect of the seepage parameter promotion was the second, and the effect of the hard brittleness index promotion was relatively poor. The hard brittleness index and water pressure parameters were positively correlated with the tangential and radial stresses in the surrounding rock, and the radial stresses were overall smaller than the tangential stresses. The deformation of the surrounding rock was twice as large as the initial one when hard brittleness damage and seepage acted together. These findings can provide a reference for the stability evaluation of the surrounding rock in tunnel shafts.

Keywords: initial water pressure; hard brittleness damage; surrounding rock; plastic zone

1. Introduction

In the construction of long highway tunnels in mountainous areas [1–3], deep shafts need to be constructed to meet the requirements of convenient construction and operational ventilation [4,5]. During shaft drilling and blasting construction, the surrounding rock is affected by two factors, groundwater seepage and hard brittleness damage deterioration. That shaft being flooded threatens the safety of construction workers [6], and the surrounding rock damage deterioration leads to the weakening of its mechanical bearing performance [7–9], both of which are related to the safe and efficient construction of deep and large tunnel shafts. Therefore, it is necessary to study the stress and deformation of a shaft's surrounding rock under seepage and hard brittleness damage conditions.

Previous researchers have reached a certain consensus on the stress and deformation characteristics of the surrounding rock in vertical shafts, but rarely considered both the

hard brittleness and seepage of the surrounding rock. Hoke–Brown carried out a systematic study of brittle damage in intact rocks, and their understanding that they gained has guided the engineering of numerous hard and brittle rocks, with a series of updates and refinements having since been made to the theory [10]. Khademian et al. [11] proposed an energy method for the quantitative calculation of rock failure in shaft construction and verified the rationality of the theoretical calculation method using UDEC numerical simulation. Akopyan et al. [12] discussed the instability mode of a shaft under the condition of unequal pressure. Based on a coupled equation of temperature and seepage, Cai et al. [13] optimized the effective thickness of the freezing of a shaft wall in the Huainan coal mine in China by using COMSOL numerical simulation technology, and they solved the problem of underground water damage during freezing construction. Sun et al. [14] used the convergence constraint method to evaluate the stability of a surrounding rock and support system. Oh et al. [15] used numerical simulation to analyze the thickness of a rock column in the middle of a New York subway tunnel to ensure the technical safety guarantee of the construction near the elevator shaft, and they proposed tunnel support measures. Zhou et al. [16] analyzed the stability of the surrounding rock during a shaft's construction by using a numerical calculation method. Kaya et al. [17], in order to study the stability of the surrounding rock of service shaft No. 1 of the longest highway tunnel in New Siegna, Turkey, calculated the distribution size of the plastic zone of the shaft wall by numerical simulation and an analytical method, and found that the two-dimensional numerical calculation results were in the best agreement through field monitoring. Based on the background of ventilation shaft construction in a Sanhejian coal mine, in Jiangsu Province, China, Hu et al. [18] explained the shaft deformation mechanism under the combined action of high geostress and fracture of the surrounding rock, and they proposed the deformation control technology suitable for safe construction. Liu et al. [19] analyzed a support problem of a shield-receiving shaft of the Yangtze River terrace, analyzed the engineering geological conditions, verified the internal force displacement of the support, and put forward the design and construction technology of a steel continuous shaft and deprecipitation support. Hollingsworth [20] analyzed the creep effect of the surrounding rock during construction according to the parameters of the shaft support structure in a salt rock layer and believed that the self-compression property of foam concrete could provide pressure-yielding space for the lining and should be the preferred material for the support structure. Zhou Xiaomin et al. [21] verified the rationality of using the elastic analysis method of surrounding rock to analyze the bearing capacity of a shaft lining through model experiments.

The above scholars have conducted a lot of beneficial work for the elastoplastic analysis of the surrounding rocks of shafts, but there are still some shortcomings. When the drilling and blasting method encounters hard brittleness in the surrounding rocks, such as granite and diorite, the hard-brittleness rock mass has the characteristics of a nonlinear stress–strain curve after strain peak and significant steep drop [22–25]. Under groundwater conditions, the excavation of underground work can be divided into three stages of pre-construction, starting construction without groundwater, and groundwater seepage during construction, and the seepage effect leads to obvious differences in stresses at each stage [26]. Deep shaft water disasters occur frequently, and it is difficult to accurately reflect the real stress and deformation characteristics of the surrounding rock by ignoring the hard and brittle damage and seepage effect in the calculation and analysis, or by only considering the seepage effect.

Based on the previous research, this article will apply the elastoplastic damage theory to establish a mechanical model considering seepage and hard brittleness damage characteristics, derive the analytical solution of the stress and plastic zone of surrounding rock, and verify the rationality of the solution. Relying on Tianshan Shengli Tunnel 2-2 shaft engineering, it will reveal the influence of hard brittleness damage and seepage parameters on the plastic zone, stress, and deformation of the surrounding rock.

2. Establishment of a Calculation Model

2.1. Mechanical Model of the Surrounding Rock in a Shaft

After the excavation of the shaft, the cross-sectional shape containing the shaft was circular, assuming that the surrounding rock conformed to an isotropic, continuous, and plastic incompressible porous medium, and that the longitudinal length of the shaft's surrounding rock was sufficient [27–29]. Initial observations were made as the following:

(1) A column coordinate system was established with the *Z* axis of the shaft, where the inner diameter is r_0, the outer diameter is r_1, the radius of the plastic damage zone is r_p, and any radius is r.

(2) The surrounding rock conformed to the Chinese code [30] grading criteria with a uniaxial compressive strength $R_c \geq 60$ MPa, defining it as a hard and brittle rock mass.

(3) When the initial geostress p_0 and the initial pore water pressure p_{w0} are infinite and the radius is greater than r_2, the water pressure is p_{w0}.

(4) The vector symbol convention states that compressive stress is positive and tensile stress is negative.

Adopting the stratigraphic structure method, the mechanical calculation model of the shaft's surrounding rock was established, as shown in Figure 1.
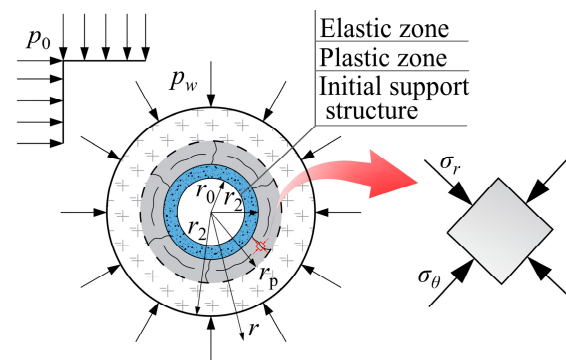
Figure 1. Mechanical calculation model.

2.2. The Surrounding Rock Yield Criterion

The Drucker–Prager criterion (referred to as the D–P criterion) is widely used in underground engineering due to its ability to accurately account for hydrostatic pressure and intermediate principal stresses, thereby explaining the yield failure of surrounding rock [31]. The D–P criterion is plotted in the π plane as shown in Figure 2.
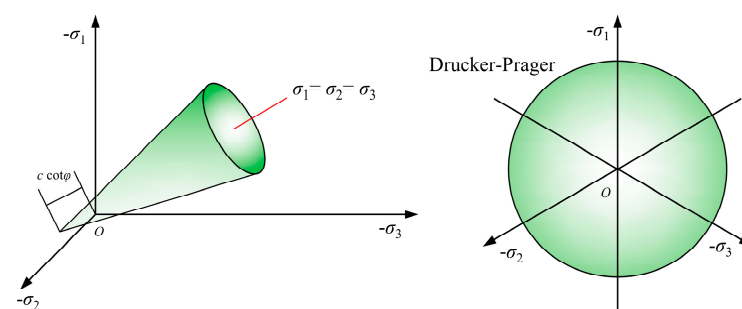
Figure 2. D-P criterion in the π plane.

This paper adopted the D–P criterion, and under the premise of positive compressive stress, the yield function can be given as [32] Equation (1):

$$f(I_1, \sqrt{J_2}) = \sqrt{J_2} - \alpha I_1 - \kappa = 0 \tag{1}$$

where f is the yield discrimination function of the surrounding rock, I_1 is the first stress invariant, J_2 is the second deviatoric stress invariant, and α and κ are the material con-

stants of the criterion. The calculation formulas for each parameter can be given as Equations (2) and (3):

$$\left.\begin{array}{l} I_1 = \sigma_1 + \sigma_2 + \sigma_3 \\ J_2 = (1/6)\left[(\sigma_1 - \sigma_2)^2 + (\sigma_2 - \sigma_3)^2 + (\sigma_3 - \sigma_1)^2\right] \end{array}\right\} \tag{2}$$

$$\alpha = \frac{\sin\varphi}{\sqrt{3}\sqrt{3 + \sin^2\varphi}} \quad \kappa = \frac{\sqrt{3}c\cos\varphi}{\sqrt{3 + \sin^2\varphi}} \tag{3}$$

where σ_1 is the first principal stress, unit MPa. σ_2 is the intermediate principal stress, unit MPa. σ_3 is the third principal stress, unit MPa. φ is the internal friction angle, unit °. c is the cohesive force, unit MPa.

Under the condition of plane strain, take a microelement of the tunnel shaft bearing a ring as shown in Figure 1. According to the physical equations of elasticity [33], the relationship between the principal stress σ_1–σ_3 in the surrounding rock and the effective stress $\sigma_r{}'$ and $\sigma_\theta{}'$ in the surrounding rock at the construction stage can be obtained by

$$\left.\begin{array}{l} \sigma_1 = \eta p_w + \sigma_r{}' \\ \sigma_2 = \mu(\sigma_1 + \sigma_3) \\ \sigma_3 = \eta p_w + \sigma_\theta{}' \end{array}\right\} \tag{4}$$

where $\sigma_r{}'$ and $\sigma_\theta{}'$ are the radial and tangential effective stresses, respectively, unit MPa. η is the effect coefficient of action of the water pressure. p_w is the calculated water pressure at the surrounding rock r, unit MPa. μ is the Poisson's ratio of the rock mass.

Assuming isotropy and isobarism in the surrounding rock, with a Poisson's ratio $\mu = 0.5$, substituting this value into Equation (4) and subsequently combining Equations (2)–(4), it can be given as Equation (5):

$$\left.\begin{array}{l} I_1 = (3/2)(\sigma_r{}' + \sigma_\theta{}') + 3\eta p_w \\ J_2 = (1/4)(\sigma_r{}' - \sigma_\theta{}')^2 \end{array}\right\} \tag{5}$$

By substituting Equation (5) into Equation (1), the circumferential effective stress can be obtained with

$$\sigma_\theta{}' = \frac{2\kappa - 6\alpha\eta p_w}{3\alpha - 1} - \frac{1 + 3\alpha}{3\alpha - 1}\sigma_r{}' \tag{6}$$

2.3. Hard Brittleness Damage Constitutive and Seepage Body Force

2.3.1. Hard Brittleness Damage Constitutive Relationship

Ref. [34] discussed a one-dimensional elastic damage constitutive model, and it can be given as Equation (7):

$$\left.\begin{array}{l} D = 0,\ \varepsilon < \varepsilon_c \\ D = (\varepsilon/\varepsilon_s)^n,\ \varepsilon \geq \varepsilon_c \\ \sigma = E(1 - D)\varepsilon \end{array}\right\} \tag{7}$$

where D is the damage variable and there is no dimensional parameter, ε is the strain of the specimen under uniaxial compression. ε_c is the peak strain, ε_s is a constant, n is the brittleness index of the rock mass, and σ and E are the elastic stress and elastic constant of uniaxial damage line, respectively, unit MPa.

Under uniaxial compression conditions, the stress–strain curve of hard and brittle rock masses is shown in Figure 3. It is not difficult to analyze that as the brittleness index increases, the curve becomes steeper and tends toward complete brittleness. From uniaxial strain to a realistic triaxial stress state [35], and when $\varepsilon \geq \varepsilon_c$, it can be given as Equation (8):

$$D' = (\varepsilon_i/\varepsilon_s)^n \tag{8}$$

where ε_i is the equivalent strain. D' is the damage variable under triaxial compression.
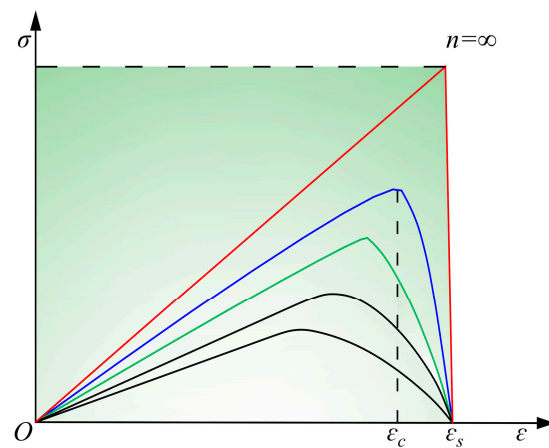
Figure 3. Constitutive damage curve of a brittle rock mass.

Under the plane strain condition, according to the geometric equation and plastic deformation volume, invariance can be given by Equation (9):

$$\left. \begin{array}{l} \varepsilon_\theta = u/r,\ \varepsilon_r = du/dr \\ \varepsilon_z = 0,\ \varepsilon_z + \varepsilon_r + \varepsilon_\theta = 0 \end{array} \right\} \tag{9}$$

where ε_θ represents the tangential strain in the plastic region. ε_r represents the radial strain in the plastic region. ε_r represents the z-direction strain. u is the displacement of the surrounding rock, unit mm.

Solving Equation (9) and considering the interface between the elastic and plastic zones, as well as the strain continuum boundary condition $\varepsilon_i|_{r=r_p} = \varepsilon_c$, the equivalent strain of the surrounding rock can be given as Equation (10):

$$\begin{aligned} \varepsilon_i &= \left(\sqrt{2}/3\right)\sqrt{(\varepsilon_z - \varepsilon_\theta)^2 - (\varepsilon_r - \varepsilon_z)^2 - (\varepsilon_r - \varepsilon_\theta)^2} \\ &= (r_p/r)^2 \varepsilon_c \end{aligned} \tag{10}$$

Substituting Equation (10) into Equation (8) resulted in a realistic three-dimensional stress damage constitutive model, and it can be given as Equation (11):

$$D' = \left(\varepsilon_c r_p^2 / \varepsilon_s r^2\right)^n \tag{11}$$

According to the Lemaitre damage strain equivalence principle [36] and the assumption of three-dimensional isotropic damage, the effective stress of surrounding rock can be given as Equation (12):

$$\sigma_\theta' = \frac{\sigma_\theta}{1 - D'},\ \sigma_r' = \frac{\sigma_r}{1 - D'} \tag{12}$$

2.3.2. Seepage Volume Force of the Surrounding Rock

After the excavation of the shaft, without the initial support structure, according to the principle of effective stress, the rock skeleton and pore water jointly shared the internal geostress of the surrounding rock [37]. The interior of a shaft lining is a free surface, and groundwater has a mainly radial laminar flow, which follows Darcy's law. The differential seepage equation can be given as Equation (13) [38]:

$$\left. \begin{array}{l} \dfrac{\partial^2 H}{\partial^2 r} + \dfrac{1}{r}\dfrac{\partial H}{\partial r} = 0 \\ H(r)|_{r=r_0} = 0 \\ H(r)|_{r=r_2} = h_{w0} \end{array} \right\} \tag{13}$$

where $H(r)$ is the head function with r as the variable, and h_{w0} is the initial head value, unit m.

The relationship between the external initial water pressure and the internal calculated water pressure under plane strain conditions is shown in Figure 4. Equation (13) was solved and the internal calculated water pressure of the surrounding rock was treated according to the general form of volume force to obtain the external initial water pressure and seepage volume force, given as Equation (14):

$$\left.\begin{array}{l} H = h_{w} \ln \frac{r}{r_0} / \ln \frac{r_2}{r_0} \\ p_{w} = \gamma_{w} H = p_{w0} \ln \frac{r}{r_0} / \ln \frac{r_2}{r_0} \\ f_r = \frac{dp_{w}}{dr} = \frac{p_{w0}}{r(\ln r_2 - \ln r_0)} \end{array}\right\} \tag{14}$$

where f_r is the seepage volume force, unit kN.
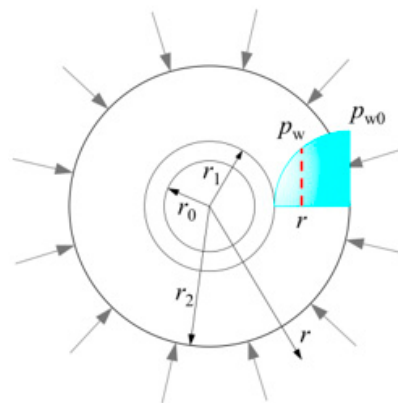
Figure 4. Seepage boundary.

3. Elastoplastic Analysis of the Surrounding Rock

3.1. Plastic Zone Stress

Taking any differential element within the surrounding rock of the tunnel shaft, as shown in Figure 5, considering the volume force of water pressure infiltration, establishing the radial equilibrium equation of elastic mechanics, it can be given as Equation (15):

$$\sum F_r = 0 \qquad (\sigma_r + d\sigma_r)(r + dr)d\theta - rd\sigma_r d\theta - 2\sigma_\theta \sin(d\theta/2)dr + \eta dp_{w}(r + dr)d\theta = 0 \tag{15}$$

where F_r is the radial resultant stress, unit MPa. $d\sigma_r$ is the radial stress of the microelement. $d\sigma_\theta$ is the tangential stress of the microelement. dp_{w} is the calculation of the water pressure of the microelement. dr is the radius of the microelement. $d\theta$ is the angle of the microelement.
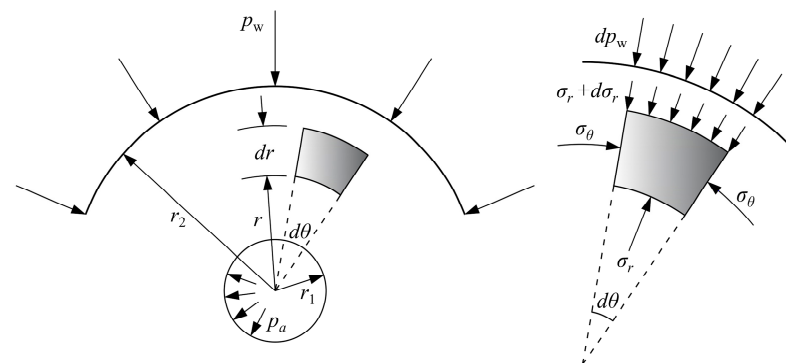
Figure 5. Force analysis of microelements.

The above equation was simplified and organized to obtain Equation (15), which is the axisymmetric equilibrium differential equation, given as Equation (16):

$$\frac{d\sigma_r}{dr} + \frac{\sigma_r - \sigma_\theta}{r} + \frac{\eta p_{w0}}{r(\ln r_2 - \ln r_0)} = 0 \tag{16}$$

Equations (6) and (12) were combined to give Equation (17):

$$\sigma_r - \sigma_\theta = \frac{6\alpha}{3\alpha - 1}\sigma_r + \frac{6\alpha\eta p_w - 2\kappa}{3\alpha - 1}(1 - D') \tag{17}$$

Equation (17) was substituted into Equation (16), the equilibrium equation, to obtained

$$\frac{d\sigma_r}{dr} + M\frac{\sigma_r}{r} = -L(r) - B(r) - N\frac{1}{r} \tag{18}$$

where $M = 6\alpha/(3\alpha - 1)$; $N = (\eta p_{w0})/\ln(r_2/r_0)$; $L(r) = \frac{\ln(r/r_1)}{r}\frac{6\alpha\eta p_{w0}}{(3\alpha-1)\ln(r_2/r_0)} - \frac{1}{r}\frac{2\kappa}{(3\alpha-1)}$; $B(r) = \left[\frac{2\kappa}{3\alpha-1} - \frac{\ln(r/r_1)6\alpha\eta p_{w0}}{(3\alpha-1)\ln(r_2/r_0)}\right]\left(\frac{r_p^2\varepsilon_c}{r^{2n+1}\varepsilon_s}\right)^n$.

Equation (18) is a first-order linear non-homogeneous equation, and it was not difficult to obtain a general solution, which can be given as Equations (19) and (20):

$$\sigma_r = Ce^{-\int \frac{M}{r}dr} - e^{-\int \frac{M}{r}dr}\int\left[L(r) + B(r) + \frac{N}{r}\right]e^{\int \frac{M}{r}dr}dr \tag{19}$$

$$\sigma_r = \frac{C}{r^M} + \frac{\kappa}{3\alpha} - \frac{\eta p_{w0}\ln(r/r_0)}{\ln(r_2/r_0)} + \frac{6\alpha\eta p_{w0}}{(3\alpha-1)\ln(r_2/r_0)} - \frac{X}{r^{2n}(M-2n)} + \frac{\ln(r/r_0)}{r^{2n}(M-2n)}Q - \frac{Q}{r^{2n}(M-2n)^2} - \frac{N}{M} \tag{20}$$

where $X = \frac{2\kappa}{3\alpha-1}\left(r_p^2\varepsilon_c/\varepsilon_s\right)^n$; $Q = \frac{6\alpha\eta p_{w0}}{(3\alpha-1)\ln(r_2/r_0)}\left(r_p^2\varepsilon_c/\varepsilon_s\right)^n$.

To solve the indeterminate coefficient C of Equation (20), a radial stress boundary condition was also required. Based on the actual construction conditions, when surrounding rock is not supported or the support lags behind, the radial stress around the shaft lining is 0, and the radial stress after the support is the support stress. The former is a special case of the latter, that is, the boundary condition is

$$\sigma_r|_{r=r_0} = p_a \tag{21}$$

where p_a is the shaft support force, unit MPa.

Substitute Equation (21) into Equation (20) to obtain $C = \left(\dfrac{p_a + \frac{Q}{r_1^{2n}(M-2n)^2} + \frac{X}{r_1^{2n}(M-2n)}}{-\frac{6\alpha\eta p_{w0}}{(3\alpha-1)\ln(r_2/r_1)} - \frac{\kappa}{3\alpha} + \frac{N}{M}}\right)r_0^M$.

Substituting the constant coefficient C into Equation (20) yielded $\sigma_r(r_p)$, and then substituting $\sigma_r(r_p)$ into Equation (17) yielded $\sigma_\theta(r_p)$. It can be seen that the stress in surrounding rock is a nonlinear function of the plastic zone radius r_p, and solving it required seeking a second boundary condition.

3.2. Stress and Displacement in the Elastic Zone

The interface between the surrounding rock in an elastic zone and a plastic zone is r_p, and the stress acting on the interface is the radial stress p_y. The elastic zone is considered as a thick-walled cylinder under uniform stress. The osmotic water pressure of the surrounding rock acts on the entire outer contour of the plane, receives uniform ground stress p_0 at

infinity, and acts on p_y near the inner radius. According to Kirsch's solution of elasticity [39], it can be given as Equation (22):

$$\left.\begin{array}{l} \sigma_{re} = p_0(1 - \frac{r_{\mathrm{p}}^2}{r^2}) + \frac{r_{\mathrm{p}}^2}{r^2} p_y + \eta \frac{dp_{\mathrm{w}}}{dr} \\ \sigma_{\theta e} = p_0(1 + \frac{r_{\mathrm{p}}^2}{r^2}) - \frac{r_{\mathrm{p}}^2}{r^2} p_y + \eta \frac{dp_{\mathrm{w}}}{dr} \end{array}\right\} \tag{22}$$

where σ_{re} is the radial stress in the elastic zone, unit MPa. $\sigma_{\theta e}$ is the radial stress in the elastic zone, unit MPa. p_0 is the geostress, unit MPa. p_y is the radial pressure at the elastoplastic interface, unit MPa.

After the excavation of the surrounding rock, the initial support structure was provided, and the mechanical state of the elastic zone of surrounding rock was regarded as a thick-walled cylinder that bore internal support resistance pressure and external ground stress pressure at infinity. The displacement of the elastic zone [40] can be given as Equation (23):

$$u_r^{\mathrm{e}} = \frac{1 + \mu}{E} \frac{(p_0 - p_a)r_1^2}{r} r > r_p \tag{23}$$

where u_r^{e} is the radial displacement in the elastic region, unit mm.

3.3. Plastic Zone Range and Displacement

At the elastic–plastic interface, satisfying $D' = 0$ and continuous boundary stress conditions, Equation (22) was superimposed to obtain

$$\left.\begin{array}{l} \sigma_{rp} + \sigma_{\theta p} = \sigma_{re} + \sigma_{\theta e} = 2p_0 + \frac{2\eta p_{\mathrm{w}0}}{r_{\mathrm{p}} \ln(r_2/r_0)} \\ \sigma_{rp} = \sigma_{re}, \ \sigma_{\theta p} = \sigma_{\theta e} \end{array}\right\} \tag{24}$$

where σ_{rp} and $\sigma_{\theta p}$ are the radial and tangential stresses in the plastic zone, respectively, as in Section 3.1.

Combined with Equations (17)–(24), the correlation equation for the plastic zone was obtained as

$$-\frac{2}{3\alpha - 1} \sigma_{rp}(r_{\mathrm{p}}, p_a) - \frac{6\alpha\eta p_{\mathrm{w}0} \ln(r_{\mathrm{p}}/r_0)}{(3\alpha - 1)\ln(r_2/r_0)} - 2p_0 - \frac{2\eta p_{\mathrm{w}0}}{r_{\mathrm{p}} \ln(r_2/r_0)} + \frac{2\kappa}{3\alpha - 1} = 0 \tag{25}$$

The above Equation (25) is still a nonlinear equation about a plastic region r_{p}. Applied to the specific engineering computational analysis, it could be solved by the iterative method or trial algorithm, and in this paper, the solution was achieved by the Newton iterative method.

Due to the negligible volumetric deformation in the plastic deformation zone and the disregard for the elastic strain in the plastic zone, its displacement was obtained [41] as the following:

$$\left.\begin{array}{ll} u_r^{\mathrm{e}} = u_r^{\mathrm{p}} & r = r_1 \\ u_r^{\mathrm{p}} = \frac{1 + \mu}{E} \frac{(p_0 - p_a)r_1^2}{r} & r_1 < r < r_{\mathrm{p}} \end{array}\right\} \tag{26}$$

where u_r^{p} is the radial displacement in the plastic zone, unit mm.

4. Project Overview and Analytical Solution Verification

4.1. Project Overview

The Urumqi to Ruoqiang Expressway is an important part of China's expressway network. Its key project is the 22.1 km Tianshan Shengli Tunnel, which is the longest highway tunnel under construction in the world. For the tunnel's construction, the construction plan of "three tunnels + four shafts" was adopted, and the construction of deep and large shafts faces huge challenges. This paper studied the 2-2 shaft, which was constructed by the drilling and blasting method. The shaft is located in the glacier hinterland 11 km north of Provincial Highway 301 in Xinjiang, China, as shown in Figure 6.
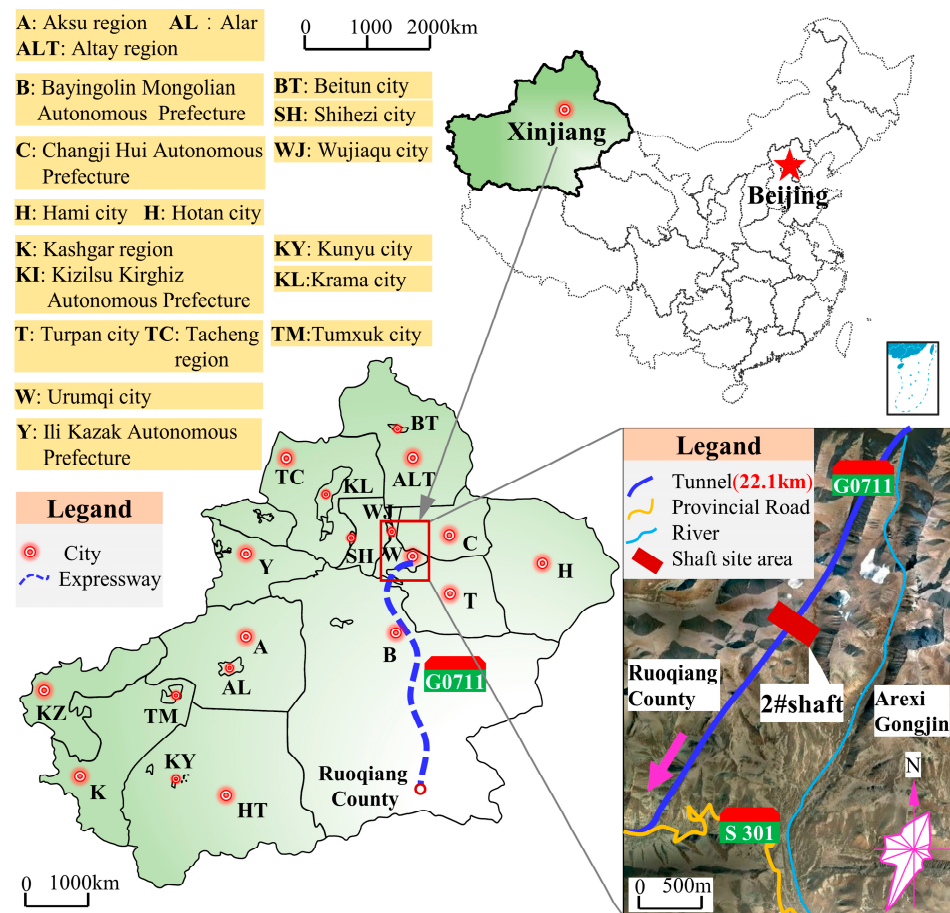
Figure 6. The specific location of the project.

The 2-2 shaft site area belongs to the tectonic denudation of mountainous terrain, at an altitude 3600 m. From October to April every year, the climate is mainly windy and snowy, and it has a typical plateau alpine environment, as shown in Figure 7a,b. The 2-2 shaft design has a depth of 704 m, diameter of 10.5 m, excavation radius $r_1 = 6.1$ m, $r_0 = 5.5$ m, and the surrounding rock has weathering that is granite- and syenite-based. During the construction of the drilling and blasting method, fissure damage occurred in the surrounding rock, and water inrush disasters occurred frequently, as shown in Figure 7c–f, and therefore, clarifying its mechanical response law was urgently needed to guide its subsequent scientific construction.

(**a**)

(**b**)

Figure 7. *Cont.*
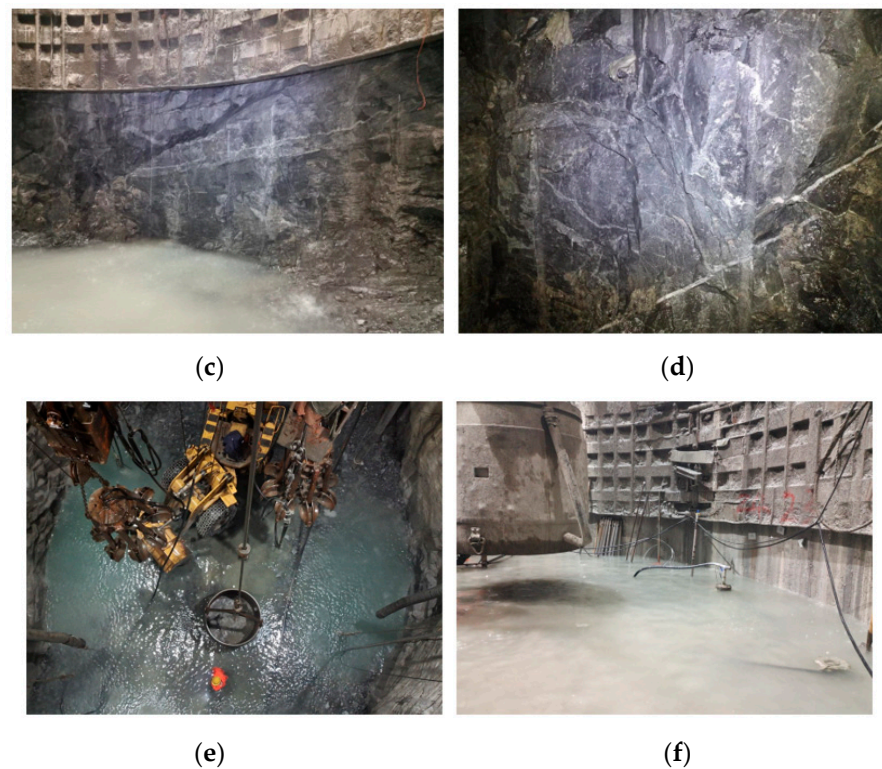
Figure 7. Tunnel and 2-2 shaft's surrounding rock seepage damage: (**a**) Tianshan Shengli Tunnel; (**b**) 2-2 shaft; (**c**) The surrounding rock seepage; (**d**) The surrounding rock damage cracks; (**e**) Water at the bottom of the shaft; and (**f**) The flooded working face.

4.2. The Surrounding Rock Parameters

4.2.1. Physical and Mechanical Parameters

With reference to the geological investigation data, the physical and mechanical parameters of the surrounding rock in the 650 m deep section of the shaft were obtained, which are listed in Table 1. As for the values of the rock brittleness index n and damage coefficient ($\varepsilon_c/\varepsilon_s$), they were calculated by using the $\sigma-\varepsilon$ relationship curve in the third equation of Equation (7), and given the values of n from 3 to 8, the corresponding values of $\varepsilon_c/\varepsilon_s$ were obtained, as listed in Table 2.

Table 1. Physical and mechanical parameters of the rock mass.

Category	γ (kN·m^{-3})	c (MPa)	φ (°)	E (MPa)	w (%)	μ
Parameter	2.5	1.0	40	5.5×10^4	0.21	0.25

Table 2. Values of the relationship between n and $\varepsilon_c/\varepsilon_s$.

n	8	7	6	5	4	3
($\varepsilon_c/\varepsilon_s$)	0.763	0.744	0.727	0.705	0.674	0.642

4.2.2. Water Pressure Parameters

With the help of the on-site monitoring method, three measuring points were arranged on average along the excavation contour of the surrounding rock at 120°, and a 1.5 MPa osmometer with a measuring range was installed, as shown in Figure 8. The installation was divided into three steps: The first step was disassembling and connecting the sensor. The packaging film of the purchased sensor was opened, and the three reserved lines of the osmometer were bundled into one cable, making sure that the length of the installation point met the requirements. The second step was wrapping half a circle of geotextile along

the side of the osmometer and gluing it with tape. The end of the osmometer was also gently glued with tape to ensure water penetration. The third step was drilling holes for installation. A diagonal hole with a diameter of 5 cm and a depth of 40 cm was drilled in the radial direction on the surface of the excavated surrounding rock. After the hole was completed, the osmometer wrapped in geotextile was inserted.
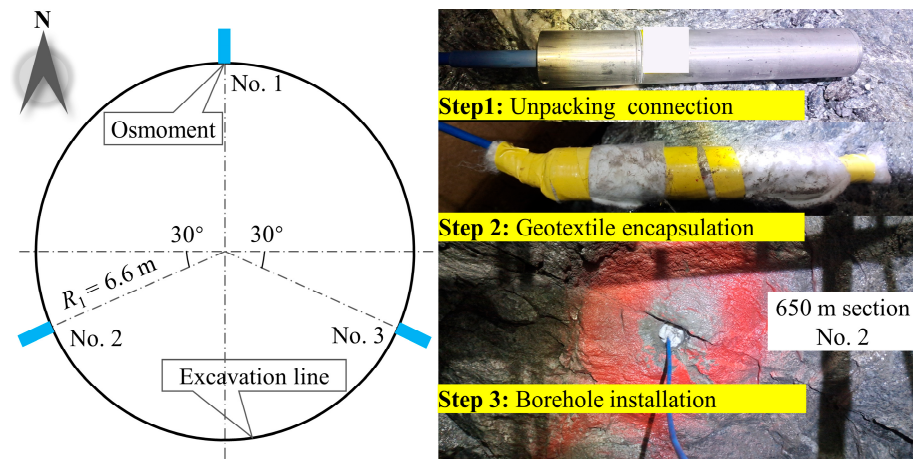
Figure 8. Water pressure monitoring plan.

Shafts have the characteristic of vertical construction face changes, and continuous water pressure monitoring is difficult to ensure, so an irregular monitoring frequency was chosen, as listed in Table 3. From the installation of the instrument on 14 September 2023 to 30 January 2024, the water pressure values at three measuring points on the 650 m deep section gradually decreased over time, with an overall water pressure value ranging from 0.01 to 0.31 MPa and an average water pressure value ranging from 0.01 to 0.227 MPa. As for the radius of water head action, it was determined through the geological survey and design report of the vertical shaft and the inquiry that r_2 was taken as 26 m. The clarity of these values was directly used for further discussion in the following text.

Table 3. Water pressure monitoring values.

Number	p_{w0} (MPa)			
	14 September	23 November	14 December	30 January
No. 1	0.22	0.12	0.14	0.01
No. 2	0.31	0.08	0.16	0
No. 3	0.15	0.17	0.11	0.02
Mean value	0.227	0.123	0.137	0.01

4.3. Reasonability Verification of Analytical Solutions

The finite element numerical simulation method and the previous research were used to verify the rationality of the analytical solution in this paper. The established two-dimensional numerical calculation model is shown in Figure 9a.

The initial water pressure p_{w0} = 0.1 MPa, and the pore pressure action coefficient η = 0.6. The crustal stress p_0 = 15 MPa, support reaction p_a = 5 MPa, and hard–brittle index n = 3 were, respectively, substituted into the analytical solution [42] and numerical calculation model for analysis. The radial stress calculation results were compared, as shown in Figure 9b.

According to Figure 9b, the adequacy of the solution was compared in terms of the curve trend and error. At the level of the overall trend, the three curves in the plastic zone area show that the farther away from the excavation contour surface, the greater the radial stress, while in the elastic zone range, the radial stress of the surrounding rock gradually tended to flatten close to the geostress, which indicates that the trend of the analytical

solution in this paper was reasonable. From the results of the error level, the overall error of the three results was less than 13%, so the results of the analytical solution of this paper were larger than the numerical calculation and smaller than the results of the literature [42]. This is mainly because the analytical solution obtained by the literature [42] only considered the seepage effect and did not take into account the hard and brittle damage of the surrounding rock, so the result was large, and the seepage and damage in the numerical calculation relied on the transmission of the mesh nodes, which led to the results of the calculations being relatively fine. Therefore, the calculation results in this paper not only reflect the surrounding rock stress state, but also the error within the acceptable range, giving them a certain degree of reasonableness.

(**a**)　　　　　　　　　　　　　　　(**b**)
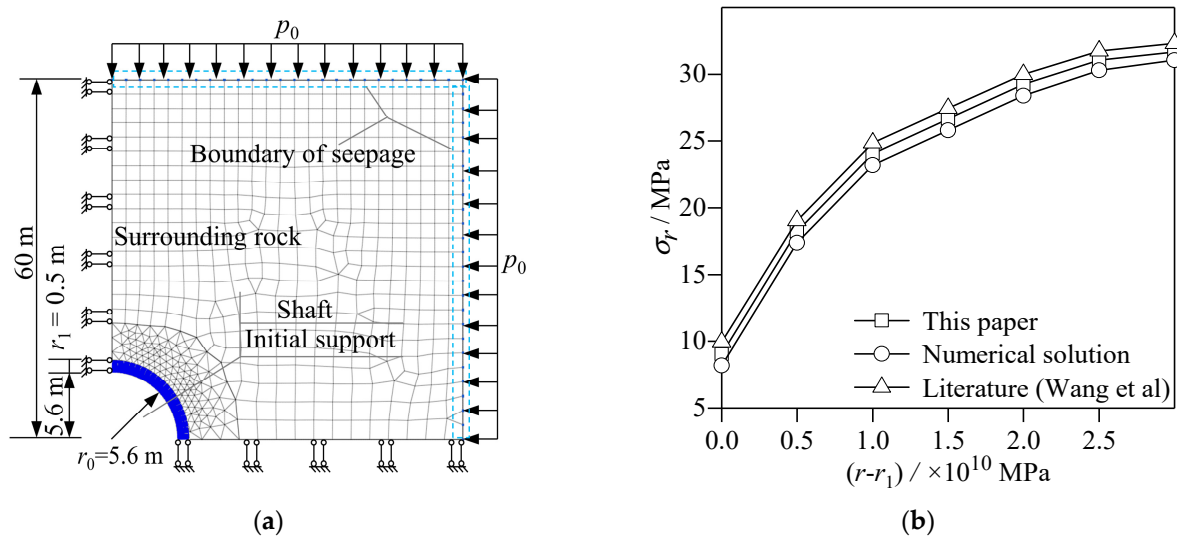
Figure 9. Numerical calculation model and comparison of results [42]: (**a**) Two-dimensional numerical model and (**b**) Comparison of solution results.

5. Results and Discussion

5.1. Influence of the Brittleness Index on the Plastic Zone of the Surrounding Rock

The seepage pore pressure coefficient $\eta = 0.6$, the initial water pressure of the surrounding rock $p_{w0} = 0.1$ MPa, the geostress $p_0 = 15$ MPa, and the supporting force $p_a = 5$ MPa were taken into account to analyze the impact of the hard brittleness index n on the plastic zone of the surrounding rock, as shown in Figure 10.

(**a**)　　　　　　　　　　　　　　　(**b**)
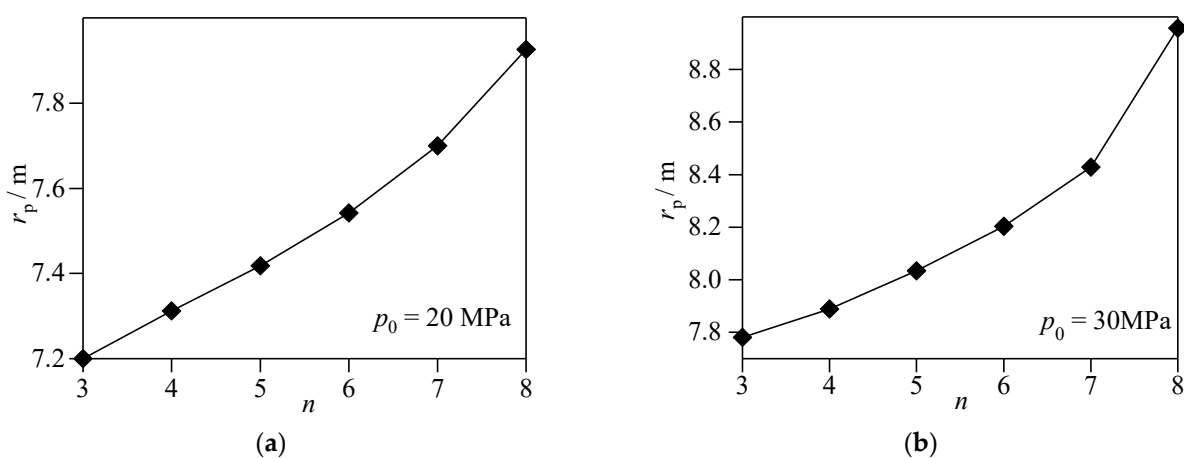
Figure 10. r_p-n relationship curve: (**a**) r_p-n relationship curve at $p_0 = 20$ MPa and (**b**) r_p-n relationship curve at $p_0 = 30$ MPa.

As can be seen from Figure 10a,b, when the water pressure was constant, the radius of the plastic zone increased with the brittleness index of the surrounding rock, and the higher the ground stress, the more significantly the radius of the plastic zone increased with the brittleness index. An increase of 1 in the brittleness index increased the plastic zone by 10 cm. The geostress increased by 10 MPa, and the plastic zone radius expanded by about 13%. Therefore, under the condition of high ground stress, when considering the brittle damage of the surrounding rock, the radius of the plastic zone underwent a significant expansion phenomenon.

5.2. The Influence of Seepage Parameters on the Plastic Zone of the Surrounding Rock

Taking the seepage pore pressure coefficient η = 0.6, the brittleness index of the surrounding rock n = 3, the geostress p_0 = 25 MPa, and the supporting force p_a = 5 MPa, the influence of the seepage parameters on the plastic zone of the surrounding rock was analyzed, as shown in Figure 11.
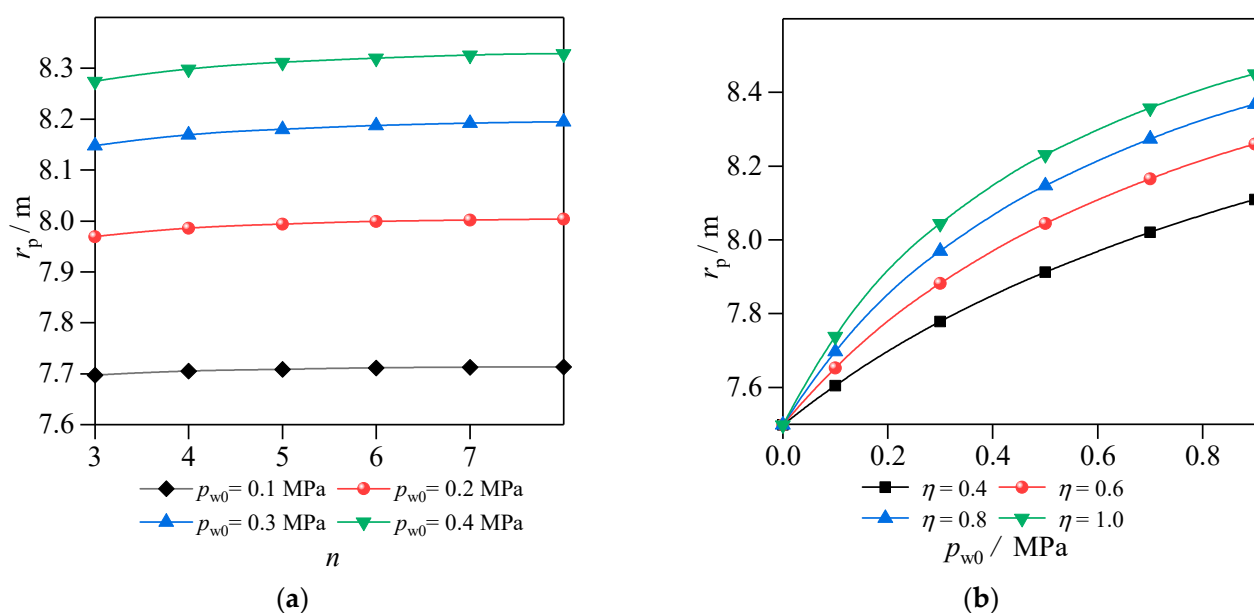
Figure 11. Relation curve between the seepage parameters and the plastic zone: (**a**) Curve of the r_p-n relationship at different p_{w0} values and (**b**) Curve of the r_p-n relationship at different p_{w0} values.

As can be seen from Figure 11a, when the hard brittleness index was constant, the radius of the plastic zone increased by about 7.2% when the initial water pressure increased from 0.1 MPa to 0.4 MPa. When the water pressure was constant, the larger the hard brittleness index, the greater the radius of the plastic zone, which is consistent with the above analytical results. In addition, when the initial water pressure increased by 0.3 MPa, the hard brittleness index increased by 3, and the radius of the plastic zone increased by about 12%. The increasing trend in the radius of the plastic zone can be considered more significant under the joint effect of the surrounding rock seepage and hard brittleness.

According to Figure 11b, after considering the seepage effect, the radius of the plastic zone and the seepage parameter showed a nonlinear growth relationship. The larger the initial water pressure, the more significant the increase in the radius of the plastic zone, and with an increase of 0.2 MPa in p_{w0}, the radius of the plastic zone increased by about 5.5%. The coefficient of pore pressure also affected the radius of the plastic zone, with an increase of 0.2 in η, and the average increase in the radius of the plastic zone was about 3.8%. It can be seen that if the seepage effect was not considered in the construction of the shaft, the design and construction support were not favourable to the stability of the surrounding rock.

5.3. Support Resistance in Relation to the Plastic Zone

Taking the pore pressure coefficient $\eta = 0.6$ and the ground stress $p_0 = 25$ MPa, the relationship between the support resistance and the plastic zone of the surrounding rock was analyzed, as shown in Figure 12.
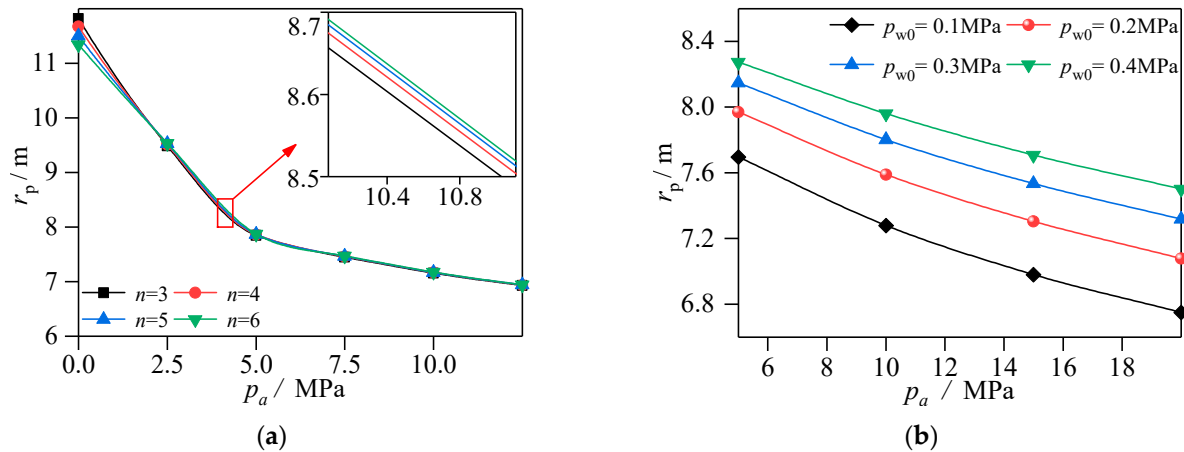
Figure 12. Relation curves between the support resistance and plastic zone: (**a**) Curve of the r_p-p_a relationship at different n values and (**b**) Curve of the r_p-p_a relationship at different p_{w0} values.

As shown in Figure 12a, when $p_{w0} = 0.1$ MPa and n was constant, with the increase in the support force, the radius of the plastic zone of the surrounding rock showed a decreasing trend. When the support force was increased to 20 MPa, and the plastic zone decreased by about 42%, the rate of decrease gradually slowed down. When the support force was constant, the larger the hard brittleness index, the larger the radius of the plastic zone. However, the contribution of the hard brittleness index to the increase in the plastic zone was insufficient to offset the suppression of the support force. The above analyses showed that even if the hard and brittle damage phenomenon occurred in the surrounding rock of the drilled shaft, timely and reasonable support measures could help to inhibit the expansion of the radius of the plastic zone and ensure the stability of the surrounding rock.

As shown in Figure 12b, when the brittleness index of the surrounding rock $n = 3$, p_{w0} was constant, and the radius of the surrounding rock plastic zone continued to decrease with the increase in the support force, increasing to 6 MPa and decreasing by about 10.5%. When the support force was constant, the greater the initial water pressure, the larger the radius of the plastic zone. Compared with the support force, the contribution of water pressure to the increase in the plastic zone was small, but its contribution was significantly higher than the hard brittleness index. The above analyses showed that it was necessary to adopt a lining for the surrounding rock community for impermeability, but without considering the brittle damage characteristics of the surrounding rock.

5.4. Stress Analysis of the Surrounding Rock

Taking the pore pressure coefficient $\eta = 0.6$, initial water pressure $p_{w0} = 0.1$ MPa, rock hard brittleness index $n = 3$, geostress $p_0 = 25$ MPa, and support resistance $p_a = 5$ MPa, the change rule of rock stress will be discussed, as shown in Figure 13.

As shown in Figure 13a, the tangential stress of the surrounding rock presented a two-stage rule of change in "increasing first, then decreasing", where the larger the brittleness index n, the larger the tangential stress. It increased from 3 to 5, and the tangential stress increased by about 5%. When the brittleness index was certain, the tangential stress showed an increasing trend in the plastic zone and a decreasing trend in the elastic zone. Overall, it was characterized by a higher tangential stress as the distance from the excavation contour surface increased. The radial stress of the surrounding rock was generally smaller than the

tangential stress, manifested by an increasing trend of the excavation contour facing inward, and the larger the brittleness index, the greater the radial stress of the surrounding rock.
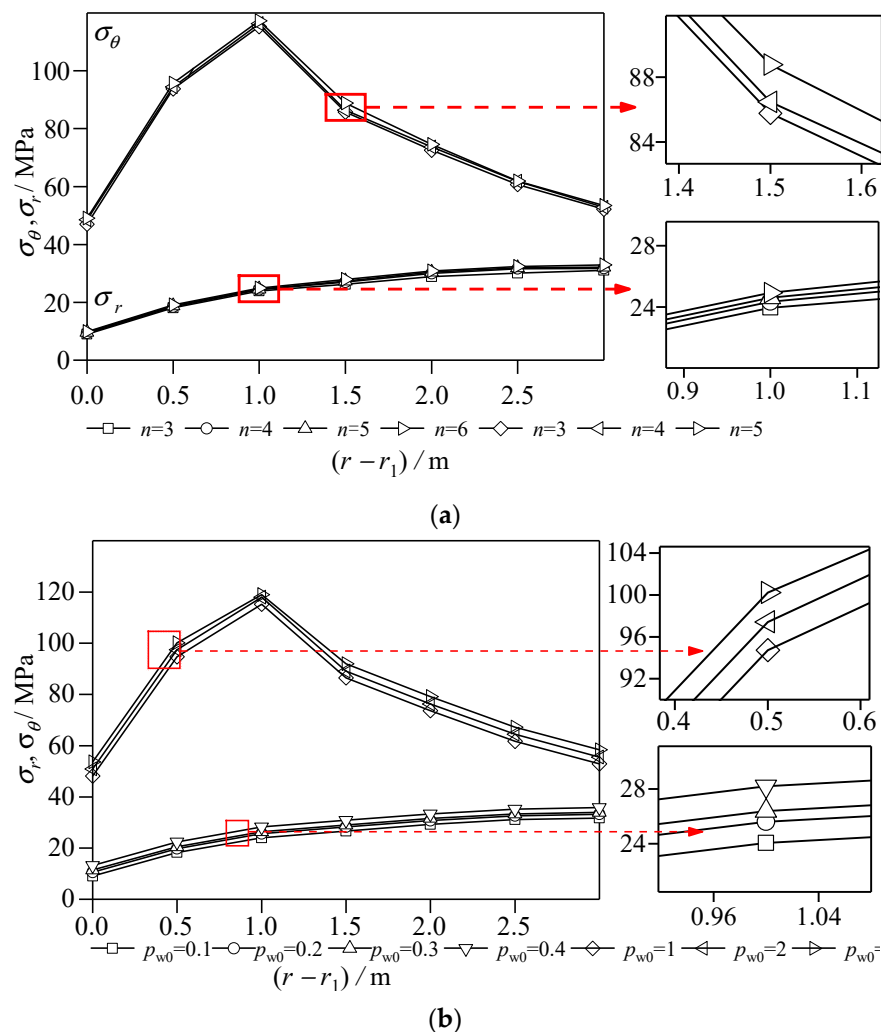
Figure 13. Relationships between the seepage and brittle parameters and the surrounding rock stress: (**a**) σ_θ, σ_r—p_a relationship curves under different n conditions and (**b**) σ_θ, σ_r—p_a relationship curves under different p_{w0} conditions.

As the brittleness index increased from 3 to 5, and the radial stress increased by about 11.1%. The radial stress did not increase all the time, but tended to stabilize away from the elastic–plastic interface in the direction of the elastic zone. This indicates that the construction principle of a "short excavation and short support" must be followed after the excavation of hard and brittle deep shafts, and the surrounding rock must be protected as much as possible, so that the exposure time after excavation is not too long, to prevent excessive tangential stress from inducing rock splitting and peeling and forming excessive rock fragmentation. At the same time, active support reinforcement measures were taken to coordinate the increase in radial stress in the surrounding rock and maintain its dynamic stability.

As shown in Figure 13b, under different initial water pressure conditions, the tangential stress and radial stress of the surrounding rock had basically the same trend, but the initial water pressure had a better sensitivity to the surrounding rock stress, and when the brittleness index increased from 3 to 5, the tangential stress increased by about 10.4% and the radial stress increased by about 44.2%. It can be seen that the key to controlling the

stability of seepage and hard-brittleness-damaged perimeter rock is anti-drainage, and it is crucial to solve the problem of anti-drainage during the construction period.

5.5. Analysis of Displacement in Plastic Zone of the Surrounding Rock

A pore pressure coefficient $\eta = 0.6$, $p_{w0} = 0.1$ MPa, brittleness index of the surrounding rock $n = 3$, geostress $p_0 = 25$ MPa, and support resistance $p_a = 5$ MPa were taken to analyze the change rule in the surrounding rock stress, as shown in Figure 14.
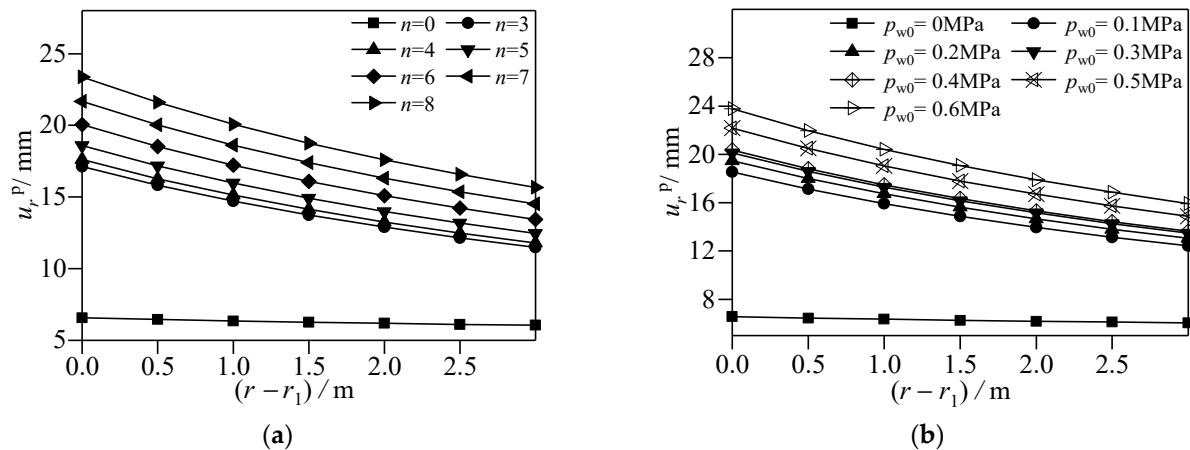
Figure 14. Relationships between the seepage and brittle parameters and shaft lining displacement: (**a**) u_r^{P} curves under different n conditions and (**b**) u_r^{P} under different p_{w0} conditions.

As shown in Figure 14a, the displacement of the plastic zone of the surrounding rock showed a decreasing trend, and the smaller the displacement of the plastic zone was from the excavation contour surface of the shaft to the interior of the surrounding rock. Considering the hard and brittle damage characteristics of the surrounding rock, the displacement of the plastic zone obviously increased by about 1.1 times as a whole. The above analyses show that in the construction and design of hard rock deep and large vertical shafts, deformation calculation of the surrounding rock without considering hard and brittle damage characteristics is on the dangerous side, and the monitoring and deformation control benchmarks should be appropriately lowered.

As shown in Figure 14b, when the initial water pressure was certain, the displacement of the plastic zone decreased from the excavation profile of the shaft to the interior of the surrounding rock. After considering the seepage characteristics of the surrounding rock, the overall displacement of the plastic zone also increased by about 0.9 times. Compared to brittle damage, the sensitivity of the surrounding rock deformation to initial water pressure parameters was slightly smaller. The above analyses showed that that the brittle damage of the rock mass was dominant, and the seepage effect was one of the reasons for the deformation of the surrounding rock after unloading during vertical shaft excavation.

In addition, the displacement variation law of the plastic zone under the combined action of hard brittleness damage and seepage was analyzed, as shown in Figure 15. It was not difficult to analyze and obtain the result that with an increase in the initial water pressure p_{w0} and hard brittleness damage index n, the displacement u_r^{P} in the plastic zone showed the trend of increasing. Considering the combined effect of hard brittleness damage and seepage of the surrounding rock, the deformation of the surrounding rock was twice as much as the original.
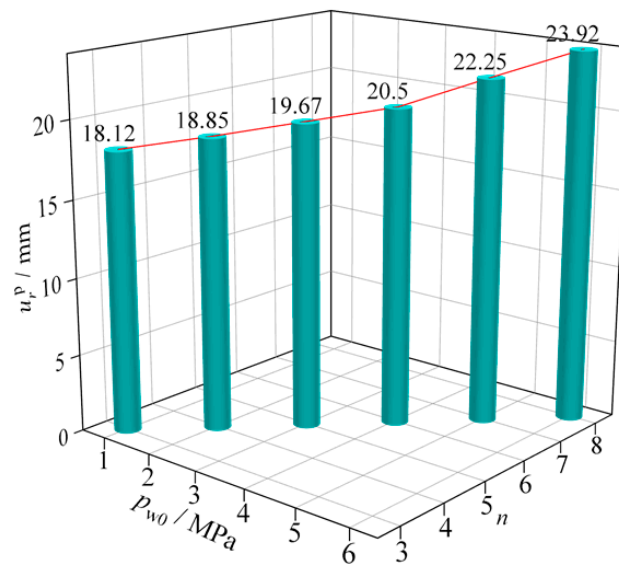
Figure 15. The impact curve of the p_{w0} and n on u_r^p curve.

5.6. Discussion

This paper focused on the stress and deformation of the surrounding rock in shafts of highway tunnels. The "strata structure" analysis method was adopted, taking into account the characteristics of the surrounding rock seepage and hard brittleness damage. An elastoplastic mechanical calculation model of the surrounding rock was established, the plastic zone and stress analysis formula of the surrounding rock were derived, and the reasonableness of the analytical solution was verified. Based on the example of the Shengli Tunnel 2-2 shaft project in Tianshan Mountain, the influence of hard and brittle damage and seepage parameters on the plastic zone, stress, and deformation of the surrounding rock of the shaft was revealed. These findings can be used as a reference for analyzing the stability and supporting the surrounding rocks of shafts in similar formations. Some of the authors' reflections are given below in order to facilitate further subsequent research.

Firstly, the rheological factor of the deep surrounding rock was not considered. The definition of a deep rock body is a rock body greater than 800 m, and the deepest road tunnel is currently 704 m, so in other words, it was the dependent project in this article. Regarding other deep projects, after considering the rheological factor, the rheological pressure will be part of the deformation pressure, and the support force calculated by using the theoretical model of this article will be increased, and the structure will be safer. However, rheology depends on a longer time period, and the secondary lining is subjected to rheological loading during the service period, so the safety reserve will be degraded. With the increase in the burial depth of the extra-long tunnel [43], hard rock deep shaft construction faces the influence of high geostress. Deep hard rock has significant unloading rheological properties, and the complex mechanical properties of the surrounding rock rheology after shaft excavation will also affect the deformation and stress distribution law of the surrounding rock [44], so the three factors of the unloading rheology, hard brittleness damage, and seepage should be taken into account in any future research.

Secondly, there was a lack of on-site monitoring data during the construction period. As we all know, the new Austrian method of tunneling follows the principle of "diligent measurement", which is achievable in horizontally driven tunnels, but almost impossible in vertically driven shafts. The authors who investigated the current stage of the shaft project literature [45,46] rarely mentioned the construction period's on-site monitoring and measurement content, perhaps because of the fact that the implementation process was relatively difficult.

Numerical simulation methods [47] may be able to solve the first problem mentioned above, and satisfactory results may be achieved by the secondary development of coupled

equations that consider all the three factors of the unloading rheology, hard brittleness damage, and seepage. As for the second problem, it is recommended that an automated monitoring method be used during the construction period in any subsequent research, combined with theoretical calculations.

6. Conclusions

This paper aimed to study the stress and deformation of a shaft's surrounding rock. First, a mechanical model of the surrounding rock with consideration of seepage and hard brittleness damage characteristics was established. Then, analytical formulas of the surrounding rock stress and plastic zone were derived to verify the rationality of the solution. Finally, the influence of hard brittleness damage and seepage parameters on the plastic zone, stress, and deformation of the shaft's surrounding rock was revealed by an engineering example. This study drew the following conclusions:

1. This paper deduced an analytical solution for determining the seepage and hard brittleness of the surrounding rock of a vertical shaft, which was not only degradable to the existing literature solution, but also agreed well with the numerical calculation results and had good extensibility and rationality. It is feasible to use it as a stress and deformation calculation for the surrounding rock of tunnel shafts.
2. Under the condition of high geostress, considering the brittleness of the surrounding rock, the radius of the plastic zone was enlarged significantly. The radius of the plastic zone increased with the increase in the initial seepage pressure and the pore pressure acting coefficient, but the increasing trend slowed down when the seepage pressure was close to the failure strength of the surrounding rock.
3. The sensitivity of the support force to restrain the increase in the radius of the plastic zone was the best, the sensitivity of the initial water pressure to the increase in the plastic zone radius was the second, and the sensitivity of the hard brittleness index to the increase in the plastic zone radius was the smallest. The lining of the surrounding rock's community impermeability principle was reasonable, but attention needed to be paid to the surrounding rock's hard brittleness damage characteristics.
4. The greater the hard brittleness index and initial water pressure of the surrounding rock, the greater the tangential stress and radial stress, but the radial stress was smaller than the tangential stress. Considering the combined effects of the hard brittleness damage and seepage of the surrounding rock, the deformation of the surrounding rock was twice as much as the original. Therefore, it was necessary to consider the hard brittleness and seepage of the surrounding rock.

Author Contributions: Formal analysis and writing—original draft preparation, Z.Z.; resources and funding acquisition, J.C.; conceptualization and methodology, T.F.; supervision and project administration, W.L.; investigation, Y.L.; validation, C.W.; writing—review and editing, J.D.; writing—review and editing, J.L.; writing—review and editing, H.W.; writing—review and editing, D.H. All authors commented on previous versions of the manuscript. All authors have read and agreed to the published version of the manuscript.

Data Availability Statement: The original contributions presented in this study are included in this article, and further inquiries can be directed to the corresponding author.

Conflicts of Interest: Authors Zhenping Zhao, Jialiang Dong, Jian Li, Heqi Wang, and Dengxia Huang were employed by the company, CCCC Central-South Engineering Co., Ltd. The authors declare no conflicts of interest.

References

1. Chen, J.; Liu, W.; Chen, L.; Luo, Y.; Li, Y.; Gao, H.; Zhong, D. Failure Mechanisms and Modes of Tunnels in Monoclinic and Soft-Hard Interbedded Rocks: A Case Study. *KSCE J. Civ. Eng.* **2020**, *24*, 1357–1373. [CrossRef]
2. Luo, Y.; Shi, Z.; Wang, C.; Chen, J. Mechanical properties of rock bolt and analysis for the full-process of sliding failure based on rock mass absolute displacement. *J. Traffic Transp. Eng.* **2022**, *9*, 490–506. [CrossRef]
3. Liu, W.; Chen, J.; Chen, L.; Luo, Y.; Shang, Q.; Zhang, L.; Gao, S.; Jia, H. A Rational Construction Method and Deformation Control System of Tunnelling in Extremely Soft and Fractured Chlorite Schist Medium. *Tunn. Undergr. Space Technol.* **2024**, *143*, 105472. [CrossRef]
4. Fang, T.; Zhao, Z.; Chen, J.; Luo, Y.; Liu, W.; Li, D.; Yu, R.; Li, J. Bearing Capacity of a Concrete Grouting Pad on the Working Surface of a Highway Tunnel Shaft. *App. Sci.* **2024**, *14*, 2933. [CrossRef]
5. Huang, M.; Yao, X.; Tan, Z.; Li, J. Research on Water Pressure Distribution Characteristics and Lining Safety Evaluation of Deep Shaft in Water-Rich, Large, Fractured Granite Stratum. *Appl. Sci.* **2023**, *12*, 7415. [CrossRef]
6. Ren, Z.; Zhang, C.; Wang, Y.; Lan, S.; Liu, S. Stability analysis and grouting treatment of inclined shaft lining structure in water-rich strata: A case study. *Geohazard Mech.* **2023**, *1*, 308–318. [CrossRef]
7. Yu, X.; Yang, Y.; Li, X.; Luo, H.; Wang, Y.; Zhang, X.; Kou, Y.; Li, H.; Zhou, Y. Cracking formation and evolution in the surrounding rock of a deep fractured rock mass roadway: A study of the 790-m level segment engineering at the Jinchuan Mine, China. *Eng. Geol.* **2024**, *331*, 107431. [CrossRef]
8. Basnet, C.; Panthi, K. Analysis of unlined pressure shafts and tunnels of selected Norwegian hydropower projects. *J. Rock Mech. Geotech.* **2018**, *10*, 486–512. [CrossRef]
9. Li, Z.; Lai, J.; Ren, Z.; Shi, Y.; Kong, X. Failure mechanical behaviors and prevention methods of shaft lining in China. *Eng. Fai. Ana.* **2023**, *143*, 106904. [CrossRef]
10. Hoek, E.; Brown, E.T. The Hoeke-Brown failure criterion and GSI—2018 edition. *J. Rock Mech. Geotech.* **2018**, *11*, 445–463. [CrossRef]
11. Khademian, Z.; Ozbay, U. Modeling violent rock failures in tunneling and shaft boring based on energy balance calculations. *Tunn. Undergr. Space Technol.* **2019**, *90*, 62–75. [CrossRef]
12. Akopyan, Z. Nonaxisymmetric loss of stability in a vertical mine shaft. *Int. J. Appl. Mech.* **1976**, *12*, 517–519. [CrossRef]
13. Cai, H.; Yao, F.; Hong, R. Multi-loop pipe freezing optimization of deep shaft considering seepage effect. *Arab. J. Geosci.* **2022**, *15*, 153. [CrossRef]
14. Sun, C.; Zhang, X.; Zhang, J. Stability Analysis of Shaft The surrounding rock and Support System in Deep Fault Fracture Zone. *J. Coal Ind.* **2013**, *38*, 587–594. [CrossRef]
15. Oh, J.; Daly, W.; Rybansky, J.; Xu, K. Numerical Analysis of shaft and Tunnel Design Adjacent toStation Cavern. In Proceedings of the GeoCongress 2012: State of the Art and Practice in Geotechnical Engineering, San Francisco, CA, USA, 25–29 March 2012; pp. 3285–3294. [CrossRef]
16. Zhou, X.; Xu, S.; Leng, X. Analysis on Mechanical Properties of the surrounding rock and Structure of Deep and Large Vertical Shaft Construction by Main Shaft Method. *Mod. Tunn. Technol.* **2019**, *56*, 325–331. [CrossRef]
17. Kaya, A.; Tarakçi, C.Ü. Stability Investigation of a Deep Shaft UsingDifferent Methods. *Int. J. Geomech.* **2020**, *21*, 05020009. [CrossRef]
18. Hu, Y.; Li, W.; Wang, Q.; Liu, S. Vertical Shaft Excavation Shaping and the surrounding rock Control Technology Under the Coupling Action of High Ground Stress and Fracture Formation. *J. Perform. Constr. Fac.* **2020**, *34*, 04020116. [CrossRef]
19. Liu, X.; Feng, X.; Lu, X.; Wu, Z.; Wang, Y. Study on Technique of Foundation Pit forShield Receiving Shaft of River-crossing Tunnel in the First Yangtze River'sTerrace. In Proceedings of the International Conference on Pipelines and Trenchless Technology (ICPTT) 2009, Shanghai, China, 18–21 October 2009; pp. 1508–1516. [CrossRef]
20. Hollingsworth, S.E.; Colbeck, A.F. Design of shaft linings to resist timedependent deformation in evaporite rocks. *Min. Technol.* **2013**, *122*, 221–227. [CrossRef]
21. Zhou, X.; Hu, Q.; Ma, C. Comparative study on influence of the surrounding rock on bearing capacity of shaft wall. *J. Coal Ind.* **2012**, *37*, 26–32. [CrossRef]
22. Yang, B.; Jiang, X.; Duan, Y. Reasonable value range of damage stress during rock brittle failure under compression. *Geomech. Geophys. Geo-Energ. Geo-Resour.* **2024**, *10*, 32. [CrossRef]
23. Zhu, G.; Feng, X.; Pan, P.; Zhou, Y.; Yang, C.; Li, Z.; Taiwakuli, Y. Real-time monitoring of the development of brittle fracture in hard rock tunnels based on physical model test. *Tunn. Undergr. Space Technol.* **2022**, *119*, 104240. [CrossRef]
24. Maleki, S.; Fiorotto, V. Hydraulic Brittle Fracture in a Rock Mass. *Rock Mech. Rock Eng.* **2021**, *54*, 5041–5056. [CrossRef]
25. Wang, P.; Xie, Y. Numerical Simulation of Fracture Failure Characteristics of Rock-Mass with Multiple Nonparallel Fractures Under Seepage Stress Coupling. *Geotech. Geol. Eng.* **2022**, *40*, 2769–2779. [CrossRef]
26. Rodríguez, C.A.; Rodríguez-Pérez, M.; López, R.; Hernández-Torres, J.A.; Caparrós-Mancera, J.J. A Finite Element Method Integrated with Terzaghi's Principle to Estimate Settlement of a Building Due to Tunnel Construction. *Building* **2023**, *13*, 1343. [CrossRef]
27. Ignaczak, J. Stress characterization of elastodynamics for an inhomogeneous transversely isotropic infinite cylinder under plane strain conditions. *Mech. Res. Commun.* **2015**, *68*, 40–45. [CrossRef]
28. Sanders, J. Nonlinear theories for thin shells, Quart. *Appl. Math.* **1963**, *21*, 21–36. [CrossRef]

29. Zhuravkov, M.; Lyu, Y.; Starovoitov, E. *Mechanics of Solid Deformable Body*, 1st ed.; Springer: Singapore; Berlin, Germany, 2023; pp. 63–68. [CrossRef]

30. People's Republic of China Ministry of Housing and Urban-Rural Development. *Standard for Engi-Neering Classification of Rock Mass*; China Planning Press: Beijing, China, 2014; pp. 8–11.

31. Yuan, X.; Liu, H.; Wang, Z. Research on the constitutive model of rock elastoplastic damage based on Drucker Prager criterion. *Geo. Mech.* **2012**, *33*, 1103–1108. [CrossRef]

32. Molotnikov, V.; Molotnikova, A. *Theory of Elasticity and Plasticity (A Textbook of Solid Body Mechanics)*, 1st ed.; Springer: Cham, Switzerland; Berlin, Germany, 2022; pp. 283–300. [CrossRef]

33. He, C.; Qi, C.; Feng, K.; Xiao, M. Theoretical analysis of interaction between surrounding rocks and linging strcture of shield tunnel based on Drucker-Prager yield criteria. *Chin. J. Theor. Appl. Mech.* **2017**, *49*, 31–40. [CrossRef]

34. Zhou, W.; Yang, G. Back analysis of elastic-brittle damage constitutive model in in-situ test hole of Laxiwa Hydropower Station. In Proceedings of the Third Congress of the Chinese Society of Rock Mechanics and Engineering, Beijing, China, 1994; pp. 543–551. (In Chinese)

35. Horii, H.; Nemat-Nasser, S. Compression-induced microcrack growth in brittle solids: Axial splitting and shear failure. *J. Geoph. Res. Sol. Ear.* **1985**, *90*, 3105–3125. [CrossRef]

36. Tumanov, A. Modification of the Lemaitre Damage Model by a Local Multiaxial Stress State Function. *Phys. Mesomech.* **2023**, *26*, 573–580. [CrossRef]

37. Zhao, Z.; Chen, S.; Chen, Y.; Yang, Q. On the effective stress coefficient of single rough rock fractures. *Int. J. Rock Mech. Min. Sci.* **2021**, *137*, 104556. [CrossRef]

38. Tiab, D.; Donaldson, E.C. Applications of Darcy's Law. In *Petrophysics (Theory and Practice of Measuring Reservoir Rock and Fluid Transport Properties)*, 3rd ed.; Gulf Professional Publishing: Boston, MA, USA, 2011; pp. 419–483. [CrossRef]

39. Rana, A.; Paul, S.K.; Dey, P. Stress field in an isotropic elastic solid containing a circular hard or soft inclusion under uniaxial tensile stress. *Mater. Today Proc.* **2019**, *11*, 657–666. [CrossRef]

40. Wang, P. Research on the Interaction between the surrounding rock and Wellbore in Deep Vertical Wells Based on Hole Expansion Theory. Master's Thesis, China University of Mining and Technology, Xuzhou, China, 2018. (In Chinese).

41. Xu, S.; Yu, M. The Effect of the Intermediate Principal Stress on the Ground Response of Circular Openings in Rock Mass. *Rock Mech. Rock Eng.* **2006**, *39*, 169–181. [CrossRef]

42. Wang, J.; Zhao, J.; Wang, L.; Wang, J.; Sun, S. Stress analysis of wellbore the surrounding rock based on unified strength theory. *J. Build. Eng.* **2009**, *26*, 105–109. (In Chinese)

43. Liu, W.; Chen, J.; Luo, Y.; Chen, L.; Zhang, L. Long-term stress monitoring and in-service durability evaluation of a large-span tunnel in squeezing rock. *Tunn. Undergr. Space Technol.* **2022**, *127*, 104611. [CrossRef]

44. Li, Y.; Zhu, W.; Fu, J.; Guo, Y.; Qi, Y. A damage rheology model applied to analysis of splitting failure in underground caverns of Jinping I hydropower station. *Int. J. Rock Mech. Min. Sci.* **2014**, *71*, 224–234. [CrossRef]

45. Feng, D.; Wu, H.; Chen, R.; Liu, F.; Yao, M. An analytical model to predict the radial deformation of the surrounding rock during shaft construction via shaft boring Machine. *Tunn. Undergr. Space Technol.* **2023**, *140*, 105321. [CrossRef]

46. Walton, G.; Kim, E.; Sinha, S.; Sturgis, G.; Berberick, D. Investigation of shaft stability and anisotropic deformation in a deep shaft in Idaho, United States. *Int. J. Rock Mech. Min. Sci.* **2018**, *105*, 160–171. [CrossRef]

47. Xie, Q.; Cao, Z.; Sun, W.; Fumagalli, A.; Fu, X.; Wu, Z.; Wu, K. Numerical simulation of the fluid-solid coupling mechanism of water and mud inrush in a water-rich fault tunnel. *Tunn. Undergr. Space Technol.* **2023**, *131*, 104796. [CrossRef]